JOURNAL OF GEOPHYSICAL RESEARCH, VOL. 112, B10306, doi:10.1029/2006JB004621, 2007

Calibrating infrasonic to seismic coupling using the Stardust sample return capsule shockwave: Implications for seismic observations of meteors

Wayne N. Edwards,[1] David W. Eaton,[1] Philip J. McCausland,[1] Douglas O. ReVelle,[2] and Peter G. Brown[3]

Received 11 July 2006; revised 9 July 2007; accepted 31 July 2007; published 18 October 2007.

[1] Shock waves produced by meteoroids are detectable by seismograph networks, but a lack of calibration has limited quantitative analysis of signal amplitudes. We report colocated seismic and infrasound observations from reentry of NASA's Stardust sample return capsule (SSRC) on 15 January 2006. The velocity of the SSRC (initially 12.5 km/s) was the highest ever for an artificial object, lying near the low end of the 11.2–72 km/s range typical of meteoroids. Our infrasonic/seismic recordings contain an initial *N* wave produced by the hypersonic shock front, followed ~10 s later by an enigmatic series of weak, secondary pulses. The seismic signals also include an intervening dispersed wave train with the characteristics of an air-coupled Rayleigh wave. We determine an acoustic-seismic coupling coefficient of 7.3 ± 0.2 μm s^{-1}/Pa. This represents an energy admittance of 2.13 ± 0.15%, several orders of magnitude larger than previous estimates derived from earthquake or explosive analogs. Theoretical seismic response was computed using in situ V_P and V_S measurements, together with laboratory density measurements from samples of the clay-rich playa. Treatment of the air-ground interface as an idealized air-solid contact correctly predicts the initial pulse shape but underestimates its seismic amplitude by a factor of ~2. Full-wave synthetic seismograms simulate the air-coupled Rayleigh wave and suggest that the secondary arrivals are higher-order Airy phases. Part of the infrasound signal appears to arise from coupling of ground motion into the air, much like earthquake-induced sounds.

Citation: Edwards, W. N., D. W. Eaton, P. J. McCausland, D. O. ReVelle, and P. G. Brown (2007), Calibrating infrasonic to seismic coupling using the Stardust sample return capsule shockwave: Implications for seismic observations of meteors, *J. Geophys. Res.*, *112*, B10306, doi:10.1029/2006JB004621.

1. Introduction

[2] On 15 January 2006 at 0956:42 UT, the Stardust sample return capsule (SSRC) reentered Earth's atmosphere after nearly 7 a in space. The SSRC was designed to return samples of interstellar dust and from comet 81P/Wild 2 but also offered an opportunity for many researchers to record its reentry as an artificial "meteor." The initial velocity of the SSRC (12.5 km/s) was the highest ever for an artificial object in Earth's atmosphere [*Mitcheltree et al.*, 1999] and at the low end of the 11.2–72 km/s velocity range typical of asteroidal and cometary meteors [*Ceplecha et al.*, 1998]. Such a planned hypersonic reentry of an object with known velocity and mass afforded an exceptional opportunity to study the excitation and propagation of hypersonic shocks from a well-calibrated, artificial "meteor." On the basis of lessons learned during reentry of the ill-fated Genesis SRC [*Jenniskens et al.*, 2006; *ReVelle et al.*, 2005], various optical, broadband photometric, spectrographic, infrasonic, and seismic instruments were deployed to record the SSRC reentry. Here we report results of an experiment to measure the acoustic-seismic coupling of the far-field shockwave, using a collocated infrasound-seismic array set up in Wendover, Utah (40.7115°N, 114.0411°W).

[3] Seismic observations of naturally occurring meteors, fireballs (bright meteors), or bolides (very bright, often detonating meteors) have been noted since the Great Siberian Meteor of 1908 [*Ben-Menahem*, 1975] but have become more commonly recognized with increasingly widespread distribution of seismograph networks. This increased seismic detection rate of fireballs coincides with a rising awareness of the utility of seismic observations for constraining the positions of meteor trajectories [e.g., *Ishihara et al.*, 2004], specific fragmentation features [e.g., *Qamar*, 1995] and the energetics of the meteor itself [e.g., *Brown et al.*, 2002]. Under favorable conditions, it may even be possible to compute approximate atmospheric velocities and perhaps

[1]Department of Earth Sciences, University of Western Ontario, London, Ontario, Canada.
[2]Atmospheric, Climate and Environmental Dynamics, Meteorological Modeling Team, Los Alamos National Laboratory, Los Alamos, New Mexico, USA.
[3]Department of Physics and Astronomy, University of Western Ontario, London, Ontario, Canada.

0148-0227/07/2006JB004621$09.00

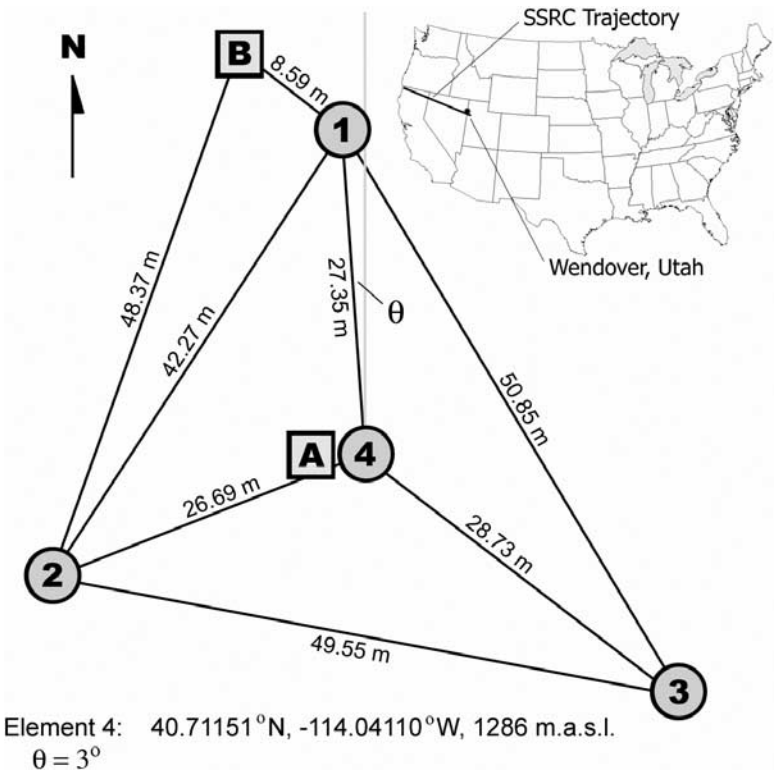

Figure 1. Layout of the colocated infrasound and seismic array at Wendover, Utah. Circles indicate the four microbarometer locations used in the infrasonic array, squares are the locations of buried seismometers A and B. Microbarometers 1–4 and seismometer A were located on/in the remains of a decommissioned aircraft runway, while seismometer B was buried within the local playa soil. Inset: Location of Wendover, UT and the ground projection of the Stardust sample return capsule (SSRC) reentry trajectory.

preatmospheric orbits from seismic data alone [cf. *Brown et al.*, 2003]. Previous seismically derived inferences of meteoroid kinematic and dynamic parameters are based on two main assumptions: (1) the observed ground motion is caused by direct loading of the surface by acoustic overpressure, as the shockwave passes over the seismograph site; (2) the efficiency of the air-to-ground coupling can be accurately approximated by extrapolating from existing surface explosion relationships.

[4] We refer to the mechanism implied by the first assumption as ''direct acoustic-seismic coupling,'' to distinguish it from the possibility of shockwave-induced seismic waves that propagate independently in the subsurface. Evidence from previous studies [e.g., *Nagasawa*, 1978, *Cevolani et al.*, 1993, *Qamar*, 1995, *Langston*, 2004] support this assumption, as typically the suspected seismic signals arrive at (or very near to) the time when an acoustic wave is predicted to arrive and/or multiple signals are observed across a seismic network with propagation velocities consistent with an airborne source soon after a meteor has been either seen or reported. Although the assumption of direct coupling often has led to location of fragmentation features and/or trajectory solutions, it has not previously been confirmed by direct observation.

[5] The second assumption has been employed for energy estimates and relies on large extrapolation of earlier empirical relations but with no validation for such high-altitude sources. Indeed, the dynamics of coupling of airwaves to the ground remains largely unexplored due to the complexity of the variables involved, including geological setting, soil properties, angle of incidence, frequency, etc. In this study we report the first colocated infrasound and seismic observations of the shockwave produced by a well calibrated, high-altitude source with a velocity similar to that of a natural meteoroid [*ReVelle*, 1976]. Our results show that seismic observations of meteoroid-induced shock waves can be approximately converted to infrasound signals and thus may form the basis for meaningful meteoroid energy calculations [e.g., *Edwards et al.*, 2006], provided that the near-surface seismic properties (particularly the shear-wave velocity) for the measurement area are well known.

2. Colocated Infrasound/Seismic Array

[6] Data for this study were collected using a temporary infrasonic and seismic array assembled at the Wendover, Utah municipal airport (KENV), located 35 km northeast of the SSRC's closest approach. The infrasound array consisted of four elements, three Chaparral Model 4 microbarometer sensors (flat response between 0.1 and 100 Hz) arranged in a triangular pattern and a fourth placed in the center (Figure 1). Each of the microbarometers was placed upon the vestiges of a decommissioned and stripped aircraft runway that consisted of the compacted gravel and crushed concrete base with its overlying asphalt removed, chosen for

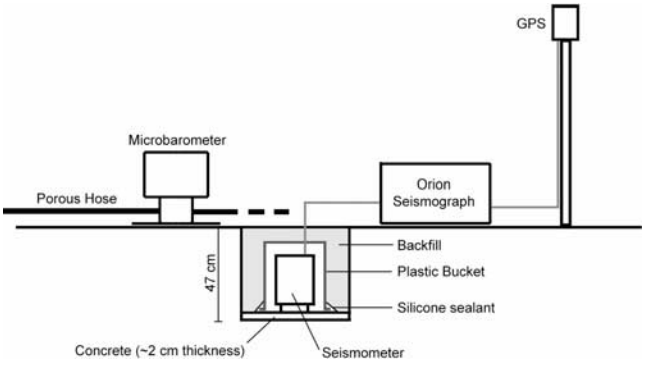

Figure 2. General setup for the seismometers at the Wendover array. At Site A, separation of microbarometer and seismometer was 0.7 m; at Site B this spacing was 8.59 m.

its flat profile and easy access. Each microbarometer was attached to six 15.24 m long porous garden hoses to provide wind and spatial filtering and was digitized at a frequency 100 Hz.

[7] The seismic component consisted of two portable Nanometrics Orion-3 seismographs, each connected to a Guralp CMG-40T three-component broadband seismometer (flat response between 0.03 and 50 Hz). Each seismometer was buried beside a microbarometer (Figure 1) to a depth of approximately 46 cm. A thin layer of concrete was set in the bottom of the hole and the seismometer was sealed beneath a plastic bucket, after which the hole was backfilled to protect it from the elements as well as isolate it from the surrounding air (Figure 2). Site A was located as close to the center element of the infrasonic array as the conditions would allow. On the basis of airport engineering data [*U.S. Department of the Army*, 1990], we estimate that a ~25–30 cm thickness of gravel remained beneath the instrument. In order to determine the possible influence of the vestigial near-surface runway material on the acoustic-to-seismic coupling site B was located just northwest of the northern infrasonic element. This seismometer was buried within the local uncompacted overburden, which consisted of a beige clay-rich playa.

3. Shockwave Measurements

[8] Observations of the Stardust shockwave (*N* wave, so named due to the N-like appearance of the pressure waveform) were made successfully on both infrasonic and seismic instruments. For a detailed analysis of the infrasonic observations, the reader is referred to *ReVelle and Edwards* [2007]. Here, particular elements of the infrasound analysis are summarized in Table 1.

3.1. Seismometer Site A

[9] Instrument response-corrected seismograms show that the first ground motion associated with the SSRC was synchronous with the 1001:04.2 UT arrival of the shockwave at the central microbarometer (Figure 3a). The signal onset is marked by a sharp positive velocity as the surface rebounds during the middle of the positive and negative phase of the shockwave pressure pulse (Figure 4a). After passage of the shockwave, a reverberation with a frequency of ~1.25 Hz was induced in the surface and is visible for up to a minute after the initial arrival. Arriving ~10 s after the *N* wave, a second, weakly dispersed arrival is evident in both the infrasound and seismic records (Figure 3a). To view the spectral contributions of this secondary arrival, an *S* transform [*Stockwell et al.*, 1996] was applied to the data. The *N* wave exhibits a dominant frequency of ~6 Hz, while the subsequent seismic wave train displays a trend from ~1.25 Hz to ~2 Hz. The secondary arrival appears to exhibit a nearly harmonic spectral pattern at ~3.5, 6, and ~8 Hz (Figure 3a).

[10] Particle-motion analysis of the *N* wave (Figure 5a) suggests an initial polarization along an azimuth of 198.4 ± 0.6 degrees. The first motion is downward and to the NE (Figure 5b), consistent with loading of the surface by a positive overpressure from the SW. The ground motion then continues in a retrograde fashion. Fitting an ellipse to this motion yields a major-axis angle of 44° ± 27°, providing an estimate of the propagation direction of the near-surface refracted *P* wave [*Langston*, 2004]. These back azimuth and incidence angles are in excellent agreement with those computed by infrasonic beam forming (Table 1) and acoustic ray tracing procedures [*ReVelle and Edwards*, 2007]. Subsequent oscillatory ground motion continues with a progressively increasing frequency from approximately 1.25 to 2 Hz. To characterize this motion, a 5-s interval immediately following the passage of the *N* wave was selected for particle-motion analysis (Figures 5c and 5d). In this case, the motion is more scattered but is approximately vertically polarized in the direction 213° ± 12° (Figure 5c). Viewed in the plane of motion (Figure 5d), a well-defined retrograde elliptical motion is apparent. The characteristics of this wave train, including its dispersed nature, vertical polarization and retrograde elliptical motion are identical to those of an air-coupled Rayleigh wave [*Ewing et al.*, 1957].

3.2. Seismometer Site B

[11] Inspection of the seismograms recorded at Site B shows a waveform that is similar to Site A (Figures 3b and 4b). Unfortunately, owing to a technical failure the east-west component of motion was rendered unusable as electronic noise every 6.8 Hz completely obscured the signal despite efforts at notch filtering. Both spectral content (Figure 3b) and motion in the vertical-northward displacement plane

Table 1. Infrasonic Measurements and Orientation of Stardust Shockwave As Recorded By Northern and Central Element Microbarometers or As Determined By Array Processing [*ReVelle and Edwards*, 2007][a]

	Central Element (Site A)	Northern Element (Site B)
Positive phase amplitude, Pa	1.068	0.938
Negative phase amplitude, Pa	−0.956	−0.733
Period, s	0.219 ± 0.003	0.191 ± 0.011
Back azimuth	200.2° ± 0.6°	
Trace velocity	535 ± 1 m/s	
Local temperature	−1°C	
Acoustic speed (ground)	331 m/s	
Angle of incidence	38.2°	

[a]Measurement band pass 0.5–40 Hz.

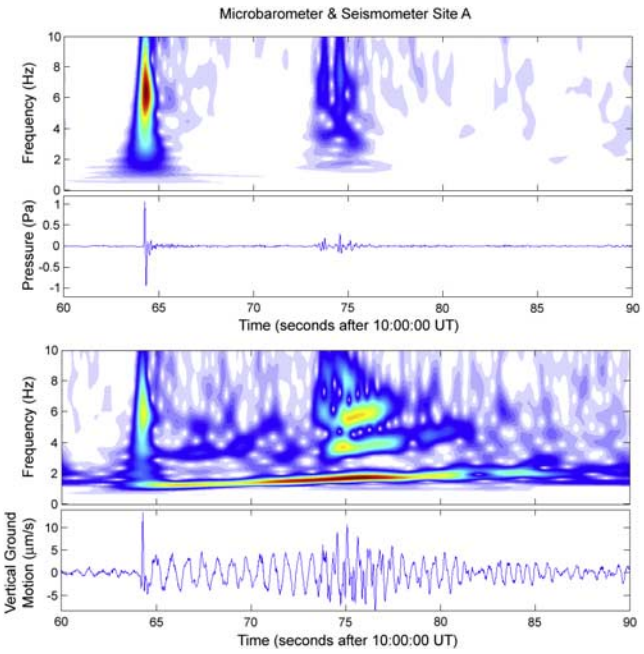

Figure 3. Infrasonic and seismic measurements of the Stardust airwave at (a) Site A and (b) Site B, with associated frequency content, determined through use of the *S* transform [*Stockwell et al.*, 1996], for the waveforms between 1 and 10 Hz. No filtering, other then clipping of spectral content below 1 Hz, has been applied.

(Figures 6a and 6b) are consistent with the polarization direction found at site A and confirm the retrograde motion of a similar air-coupled Rayleigh wave in the clay-rich playa. Indeed, the similarity between particle motions, spectra, and vertical channels at both sites suggests that the thin layer of the gravel/crushed concrete runway base had negligible affect on the ground motion; thus the response of Site A is dominated by the properties of the underlying playa. This apparent seismic transparency of the runway base material is not surprising, as the wavelength of the airwave (~66 m at ground level) is much larger than the thickness of the runway base material (<1 m).

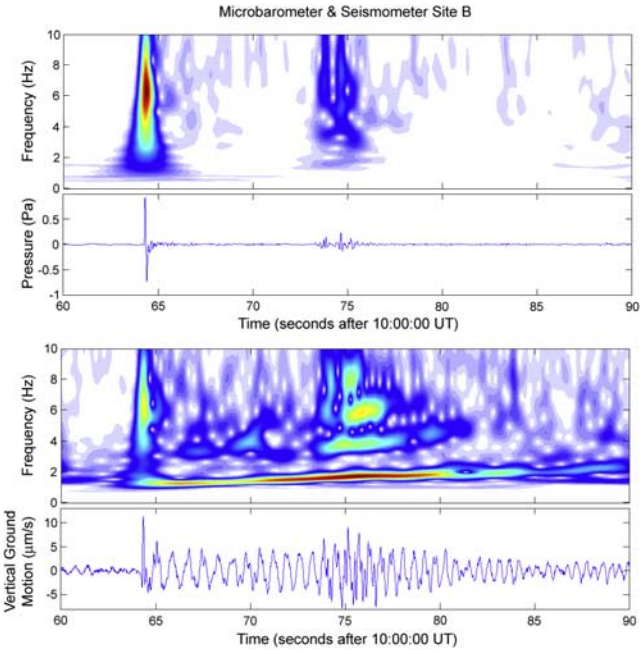

Figure 3. (continued)

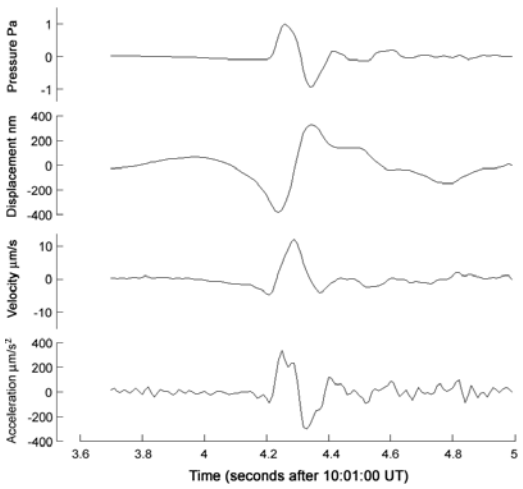

Figure 4. Comparison of response to infrasonic overpressure (top) of arriving *N* wave in terms of vertical displacement, velocity and acceleration for (a) Site A and (b) Site B. A third-order Butterworth zero-phase band-pass filter was applied between 1.5 and 30 Hz to reduce subsequent induced ground roll for both signals.

4. Acoustic-Seismic Coupling

[12] Peak vertical-component amplitudes (displacement, velocity, acceleration) recorded at Site A and Site B are given in Table 2. These observations of ground motion, along with airwave pressure measurements from the associated microbarometers, enable determination of the acoustic-to-seismic coupling efficiency as well as the acoustic-to-seismic transfer coefficient (Table 3). Previous

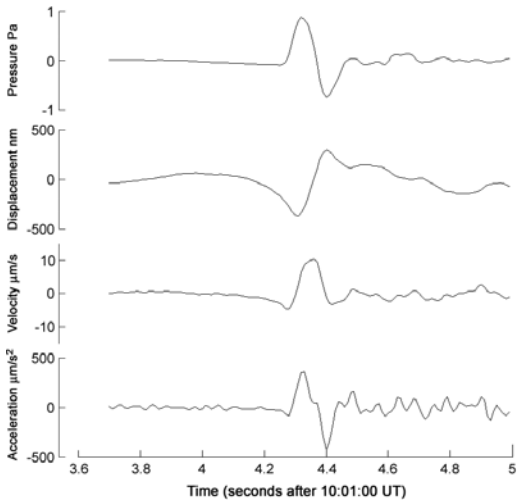

Figure 4. (continued)

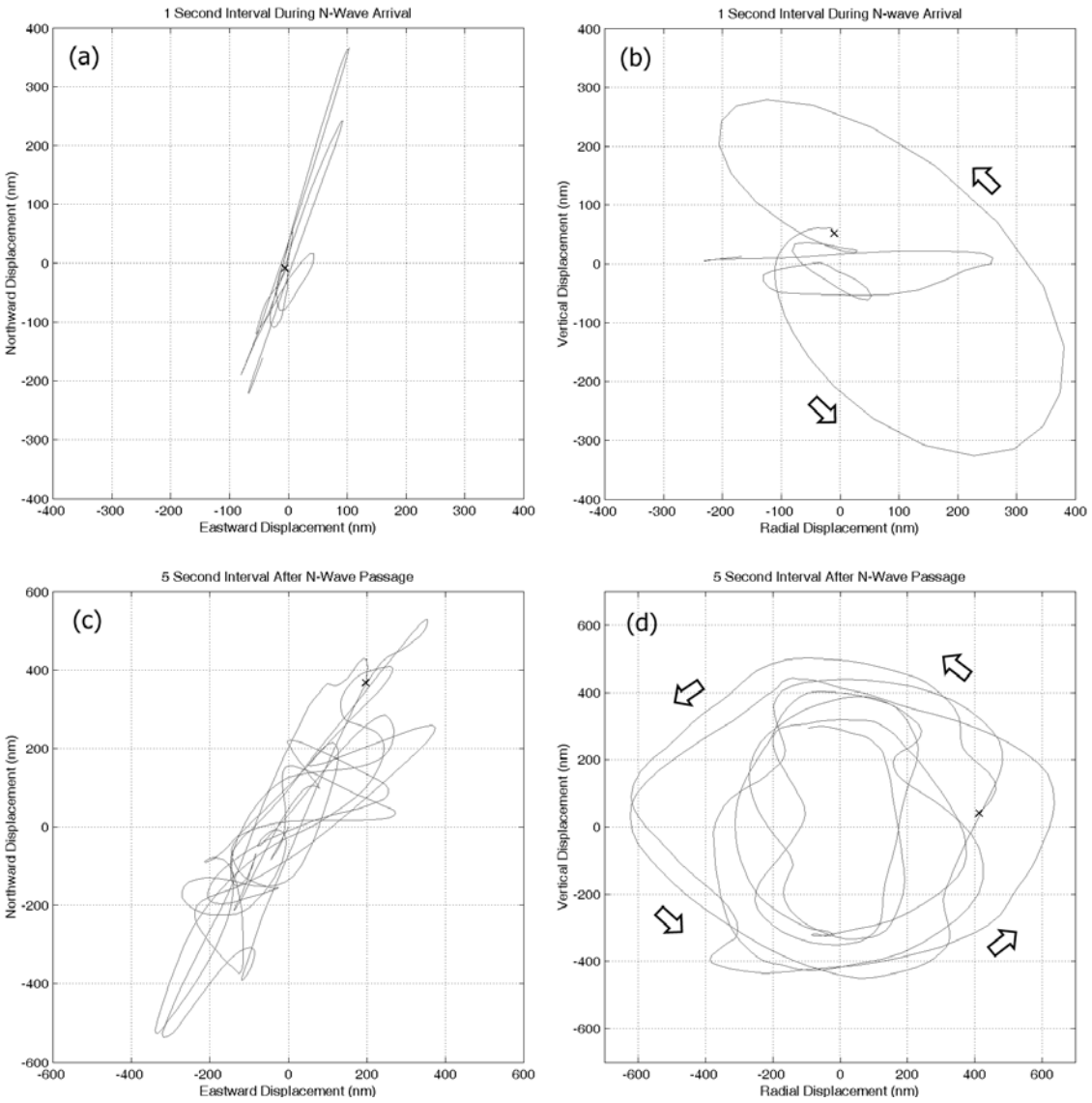

Figure 5. (a) Overhead and (b) side view of 1 s of particle motion induced during the passage of the Stardust shockwave. Azimuth of arriving signal: 198.4 ± 0.6 degrees, Incidence: 44° ± 27°, third-order Butterworth zero-phase band-pass filter applied between 2 and 30 Hz. Views (c) overhead and (d) side view are of the 5 s interval of particle motion immediately following passage of the shockwave. The shockwave has initiated ~1.25 Hz retrograde elliptical motion, polarized along the direction of the incident wave or an air-coupled Rayleigh wave (a third-order Butterworth zero-phase band-pass filter applied between 0.5 and 30 Hz). Black crosses mark initial positions of the ground motion segments.

authors who lacked colocated acoustic and seismic equipment have attempted to constrain these parameters using empirical earthquake magnitude relationships [*Hildebrand et al.*, 1997] or chemical or nuclear explosive analogs [*Brown et al.*, 2002], reaching estimates of the ratio (admittance) of acoustic to seismic energy between 10^{-4} and 10^{-7}. In the present study, direct measurement of the coupling efficiency can be determined simply by calculating the ratio of kinetic energy density in the air and ground:

$$E_{A-S} = \frac{{}^1\!/_2 \rho_{soil} v^2}{{}^1\!/_2 \rho_{air} U^2} \tag{1}$$

where ρ_{soil}/ρ_{air} and v/U are the densities and peak particle/molecular velocities of the ground and air, respectively. Molecular velocity of the air is calculated by dividing the observed pressure by the local acoustic impedance. It can be shown that this is mathematically identical to taking the ratio of kinetic energy density in the ground to the strain energy density of air:

$$E_{A-S} = \frac{{}^1\!/_2 \rho_{soil} v^2}{{}^1\!/_2 \sigma_{ij}^{air} \varepsilon_{ij}^{air}} \tag{2}$$

where σ_{ij} *and* ε_{ij} are the stress (i.e., pressure) and strain (i.e., compression) tensors, respectively.

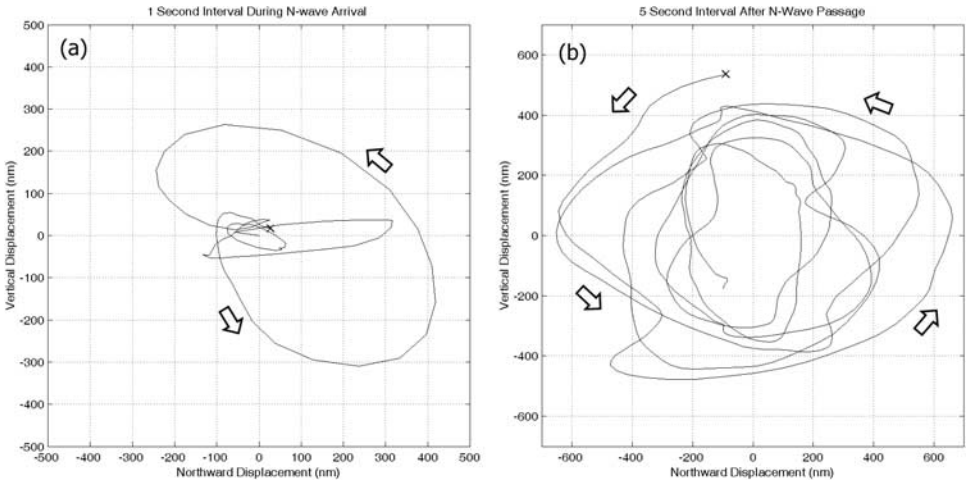

Figure 6. Particle motions in the vertical-northward displacement plane for Site B, (a) 1 s interval during *N* wave arrival, (b) during a 5 s interval after *N* wave passage. Motions are consistent with arrival direction found at Site A and show similar retrograde motion of an air-coupled Rayleigh wave.

[13] Using the measurements of Tables 1 and 2 and densities for the soil and air of 2020 kg/m^3 and 1.107 kg/m^3, respectively, we find an average acoustic-to-seismic efficiency of 2.13 ± 0.15% for the Stardust shockwave. This is significantly larger than previous estimates cited above. We remark that since only the vertical seismic amplitude component is tabulated, an effective geometrical correction factor of $1/\cos(\theta_1)$ has been applied (to account for the nonvertical angle of the transmitted *N* wave) by using the three dimensional peak velocities.

5. Soil Properties and Velocities

5.1. Laboratory Measurements

[14] Bulk elastic properties of the near surface at Wendover are required in order to model the seismic response. The natural soil (overburden) at the location of the temporary Wendover infrasound/seismic array is a clay-rich playa. Thumb-sized ~0.030 kg samples were taken during the reentry observations on 14 January 2006 at four depths from within the hole excavated for seismometer Site B (Table 4). To assess any changes due to seasonal variations in soil moisture, a second set of depth samples was taken during the shallow seismic refraction survey on 11 April 2006. Care was taken to collect undeformed, intact samples of the soil. In general, the topmost 0.10 m of the profile consisted of cohesionless, loose pebbles, and sand, whereas the remaining profile to 0.5 m depth was a massive, firm, and damp playa that was increasingly resistant to the shovel with depth.

[15] The soil grain size distribution was determined using the gravitational settling method within a sodium pyrophosphate (0.5%) solution to deflocculate clays [*American Society for Testing and Materials*, 1972]. Two replicate 0.050 kg samples provided a grain size distribution of 16% sand (>0.02 mm), 68% silt (>0.002 mm), and 16% clay-sized grains (<0.002 mm). Grain densities were measured in their initial, wet condition and then in their later dried condition to estimate the original pore water content. Grain density was measured for soil samples using a Quantachrome Multipycnometer using laboratory grade helium as the pressurized gas [*Tamari*, 2004]. Initial "wet" sample grain density measurements were made shortly after sample collection. Dry measurements were made a few weeks afterward. Initial grain density measurements reveal a lack of variation with depth. After drying, the measured grain densities for all samples approach 2700 kg/m^3, that of the silicate minerals present in the soil (Table 4). In all samples, the mass and volume of material lost during drying gives a density of 1000 kg/m^3, consistent with simple pore water loss.

[16] From these bulk and grain density measurements we conclude that the in situ Wendover playa has a porosity of ~40% and that this was fully saturated with water at the times of both the Stardust SRC reentry and the subsequent

Table 2. Seismic Measurements of the Ground-Coupled Stardust Shockwave at Sites A and B[a]

	Site A	Site B
Peak negative displacement, nm	−327	−310
Peak positive displacement, nm	279	263
Peak positive velocity, μm/s	10.98	9.32
Peak negative velocities, μm/s	−5.39 : −5.05	−5.14 : −4.45
Peak positive acceleration, μm/s^2	321	354
Peak negative acceleration, μm/s^2	−301	−426
Shockwave period, s	0.165 ± 0.003	0.144 ± 0.011
Air-coupled Rayleigh wave period, s	0.803 ± 0.043	0.803 ± 0.045
Signal duration, s	~60	~60

[a]Vertical channel only. *N* wave band pass 2–30 Hz, Rayleigh wave 0.5–30 Hz.

Table 3. Acoustic-Seismic Coupling Efficiencies Observed in the Clay-Rich Soil at Wendover, Utah, for the Stardust Shockwave[a]

Ground Motion Measure	Coupling Transfer Coefficient	Energy Coupling Efficiency
Displacement	−322 ± 15 nm/Pa	
Velocity	7.3 ± 0.2 μm s^{-1}/Pa	2.13 ± 0.15 %
Acceleration	393 ± 65 μm s^{-2}/Pa	

[a]The shockwave incidence angle was 38.2° from the vertical.

Table 4. Measured Bulk Properties of Depth Profile Samples From the Clay-Rich Soil at Wendover, Utah[a]

Depth	Initial Mass, kg	Grain Density, kg/m^3	Dry Mass, kg	Dry Grain Density, kg/m^3
		15 January		
0.18 m	0.01376	1980 ± 00	-	2680 ± 20
0.22 m	0.00712	2130 ± 10	0.00599	2620 ± 40
0.30 m	0.01455	2040 ± 00	0.01157	2690 ± 10
0.34 m	0.00922	1910 ± 10	-	-
		11 April		
0.10 m	0.02847	2070 ± 00	0.02312	2700 ± 00
0.15 m	0.01816	2060 ± 10	0.01469	2740 ± 00
0.20 m	0.01802	2070 ± 00	0.01461	2700 ± 10
0.30 m	0.01344	2030 ± 10	0.01063	2690 ± 10
0.40 m	0.01970	1970 ± 00	0.01516	2710 ± 10

[a]Formal error on the grain density measurements only exceeds ± 10 kg/m^3 as noted. Final uncertainties in density are based upon the standard deviation amongst all samples for a particular sampling date.

shallow seismic survey. The saturated clay-rich soil has an overall density of ca. 2020 kg/m^3.

5.2. Seismic Refraction Survey

[17] Near-surface and subsurface velocities at the temporary infrasound/seismic array site were estimated from data gathered during a shallow seismic refraction survey. The general procedure for the refraction survey is based on *Hunter et al.* [1998]. The survey was carried out on 11 April 2006 using a Geometrics Geode engineering seismograph system and a 24-channel geophone spread, laid out in two parallel 55 m lines with 12 horizontal and 12 vertical geophones placed side by side at 5 m intervals. The source consisted of an 8-pound (3.6 kg) sledge hammer striking a 0.5 m length of steel I-beam aligned with the geophone spread. The I-beam was struck in three directions: (1) perpendicular to the line, to generate positive-polarity SH wave signals; (2) perpendicular to the line in the opposite direction, to generate negative-polarity SH signals; (3) vertically, to generate *P* wave signals. For each source position and polarity, six sets of traces were acquired and stacked to improve the signal-to-noise ratio. This procedure was repeated at positions 5 and 30 m from both the first and last geophones in the spread to obtain extended, reversed refraction coverage.

[18] The best results were obtained using the horizontal geophones, so the vertical component data were not used for further analysis. In addition to *P*, *S*, and surface waves (ground roll), the airborne acoustic waves produced by the hammer strikes were also recorded (Figure 7). Spectral analysis shows that the much higher frequency acoustic waves (200–800 Hz) are easily filtered from the data, allowing accurate measurement of both the acoustic and seismic velocities at the time of the survey (Figure 7b). Following *Hunter et al.* [1998], *P* wave signals were enhanced by summing the two oppositely polarized horizontal records, resulting in constructive interference of the *P* waves and destructive interference of the *S* waves. Conversely, subtraction of the records was used to enhance the *S* wave signals. This approach allowed more precise determination of the wave arrivals (Figures 7c and 7d). After filtering between 20 and 150 Hz, the first breaks of the *P* and *S* waves on the respective enhanced records were picked. Velocities were then obtained from the time picks by linear regression.

[19] *P* wave (compressional) velocity, V_P, in the playa appears constant at 1344 ± 73 m/s. The *S* wave (shear) velocity, V_S, is slightly more complex, consisting of an upper and lower layer (Figure 7d). Equal apparent velocities and cross-over distances to within regression uncertainty on the reversed profiles show that the top of the lower layer is flat-lying on the scale of the survey. The top layer extends to ~5.5 m depth, as determined from the velocity crossover distances, and has a very low V_S of 178 ± 6 m/s, roughly half that of the acoustic speed in air. The underlying layer also has a low V_S (288 ± 21 m/s) but extends to an unknown depth. Despite extending the hammer source to its maximum extent at a position 65 m away from the first geophone (in order to sample velocities deeper into the subsurface), no other crossover was observed, suggesting that the lower layer extends to a depth of at least ~30–40 m. This layer is underlain by carbonate bedrock [*McCollum and Millar*, 1991].

6. Theoretical Predictions

[20] *Ben-Menahem and Singh* [1981] derived a formula for the case of a planar interface between fluid and elastic half-spaces. In this treatment the incident airwave is approximated as a plane wave,

$$\Delta p = P_0 e^{i\omega(t - x/\hat{c})} \tag{3}$$

that strikes the surface at an angle, θ (Figure 8). Subject to the boundary conditions of continuity of vertical displacement and stress, and zero horizontal traction, the vertical ground motion induced by the incident airwave is given by:

$$v_z = \frac{P_0 \hat{c} e^{\frac{-i\pi}{2}}}{2(\lambda + \mu)} \left(\frac{\lambda + 2\mu}{\mu} \right) e^{i\omega(t - x/\hat{c})} \tag{4}$$

where Δp is the airwave overpressure, P_0 it the maximum amplitude of the airwave in Pa, $\hat{c}$ is the horizontal velocity across the surface in m/s, and λ and μ are the Lamé parameter and shear modulus of the soil in Pa, respectively.

[21] This formula predicts that the airwave should couple directly to the ground, producing ground motion with a 90° phase shift and amplitude proportional to the overpressure. The constant of proportionality is defined by the elastic properties of the surface material. Previous authors have confirmed the presence of a phase shift using seismic observations of shockwaves produced by the space shuttle and supersonic aircraft [e.g., *Kanamori et al.*, 1991, 1992; *Cates and Sturtevant*, 2002], a result confirmed again in this study (Figures 4a and 4b).

[22] The Stardust shockwave observations provide the first opportunity to verify the accuracy of equation (4) for an airwave with low fundamental frequency and high source height, analogous to that expected from meteor-generated shockwaves. We used the trace velocity (apparent horizontal velocity) of the airwave from the infrasound array (Table 1) and the Lamé parameters (λ = 2.70 ± 0.30 GPa, μ = 49.1 ± 3.3 MPa) computed from the refraction and soil measure-

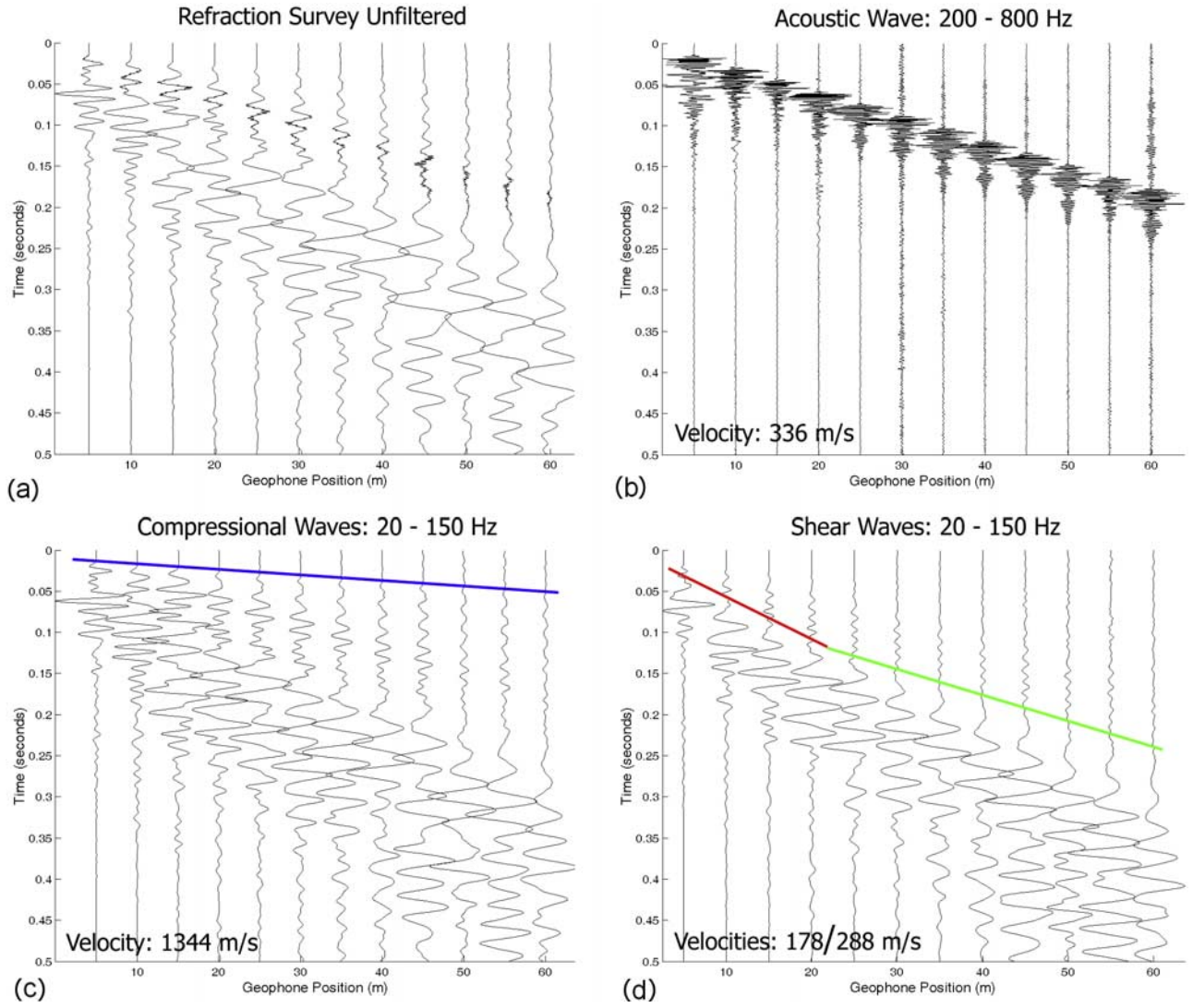

Figure 7. Shallow refraction survey of the salt flat playa at KENV, Wendover, Utah. (a) Raw unfiltered data, (b) 200–800 Hz band-passed data showing acoustic wave produced by hammer strikes. (c) 20–150 Hz band-passed data enhancing *P* waves. (d) 20–150 Hz band-passed data enhancing *S* waves. Note that shear waves in the playa propagate more slowly then than that of the acoustic waves.

ments. On the basis of equation (4), these yield a predicted air-to-ground coupling coefficient of 4.26 ± 0.16 μm s^{-1}/Pa. In Figure 9, the observed ground-coupled shockwave from Site B is plotted alongside the ground coupled wave theoretically predicted by equation (4). Although the remaining air-coupled Rayleigh wave is not explained by this simple model, the initial impulse shockwave is very well matched.

[23] Equation (4) implies a strong sensitivity to V_S of the near-surface but exhibits relative insensitivity to V_P. This sensitivity was also noted previously by *Langston* [2004]. For example, in order to match the observed seismogram within the uncertainty limits, a reduction of just 42 m/s (24%) in V_S is required. On the basis of the refraction survey observations, it is unlikely that V_S of the topmost playa layer is this slow, even accounting for possible ambiguities in *S* wave arrival picks. We conclude therefore that air-ground coupling is enhanced by another mechanism

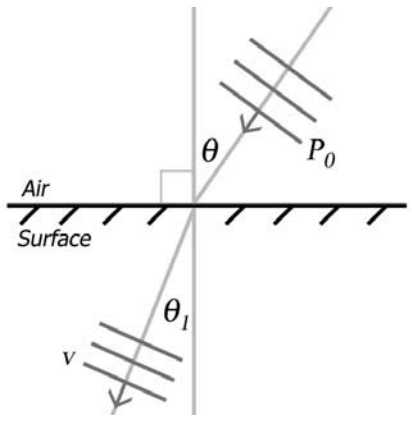

Figure 8. Air-to-ground coupling model of *Ben-Menahem and Singh* [1981]; fluid-solid half-spaces with welded contact boundary conditions.

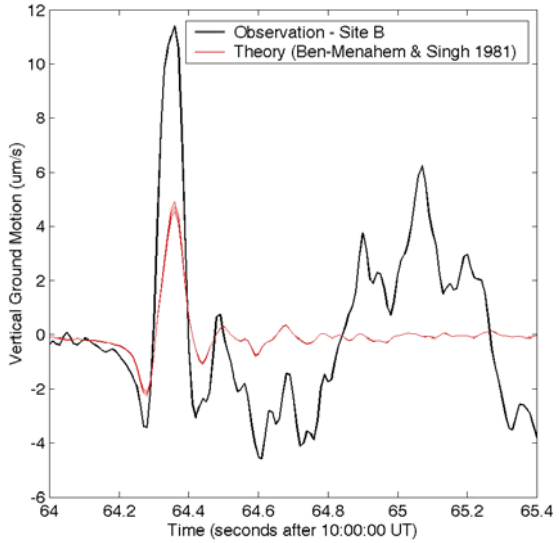

Figure 9. Vertical channel synthetic seismogram and observation comparison for Site B after applying *Ben-Menahem and Singh* [1981] theory (equation (4)) to the observed infrasonic airwave. Initial shockwave is well reproduced, though with roughly half the amplitude, while the air-coupled Rayleigh wave is not due to simplicity of the model.

that is not considered in the *Ben-Menahem and Singh* [1981] formulation.

7. Modeling the Air-Coupled Rayleigh Wave

[24] Equation (4) correctly predicts the pulse produced by direct coupling of the shockwave, but fails to reproduce the strong reverberations of the air-coupled Rayleigh wave. In order to explain the observed air-coupled Rayleigh wave train, we attempt to model the arrival with synthetic seismograms calculated using a numerically stable reflectivity algorithm developed by *Wang* [1999]. Because the thickness of the lower playa layer could not be determined from the seismic refraction survey, some other constraint is required in order to specify the Earth model. For the model parameters in Table 5, the phase velocity function $c(f)$ of the fundamental-model Rayleigh wave has a relatively simple sigmoidal shape, with low-frequency and high-frequency asymptotic limits equal to the shear-wave velocity of the bedrock and shallow playa layer, respectively. Between these asymptotic limits, $c(f)$ depends strongly on the total thickness of the overburden (Figure 10a) and hence the thickness of the lower playa layer. To determine which phase velocity curve is correct, we estimated the fundamental-mode Rayleigh wave phase velocity by measuring the average Fourier phase difference ($\Delta\varphi$) between sites A and B. The two sites are separated by a distance less than one wavelength, L, so the phase velocity is given by:

$$c(f) = (2\pi)^{-1} f L \cos\psi \Delta\varphi \qquad (5)$$

where ψ is the angle between the wave propagation vector and the line AB connecting the two sites. Applying this method in the frequency band 1.35–1.7 Hz, where the fundamental Rayleigh wave dominates (Figure 3), yields an average phase velocity of 447 ± 22 m/s. Comparing this measurement with the Rayleigh wave phase velocity curves in Figure 10a, we estimated a lower soil layer thickness of ~90 m.

[25] Group velocities calculated for a model with this lower playa layer thickness are shown in Figure 10b. Unlike the phase velocity, the group velocity curves contain local maxima and minima, referred to as Airy phases [*Aki and Richards*, 1980, p. 267]. A maximum-time Airy phase associated with each mode (n = 0, 1, 2, 3) occurs at different frequencies, all propagating at a similar group velocity of ~120 m/s. This similarity in group velocity implies a roughly synchronous arrival of the associated wave pulses. Because Airy phases are typically associated with large-amplitude arrivals, we propose that the behavior of the S spectra of the observed seismograms in Figures 3a and 3b, in which distinct, dispersive wave trains are terminated by large-amplitude arrivals that are localized in time and frequency, reflects the presence of multimodal Airy phases.

[26] Synthetic seismograms were computed using a similar four-layer model. The (air) layer at the top of the model is treated as a fluid-elastic half space with V_P = 331 m/s, V_S = 0 and ρ = 1.0 kg/m^3, while the remaining layers are assigned values as described above. The source is represented as a purely explosive point source with an impulsive source-time function and a seismic moment of $M_0 = 1.851 \times 10^7$ N-m, consistent with conversion of 10% of the available kinetic energy to acoustic shockwave energy along the segment of the Stardust SRC trajectory detected by our instruments [*ReVelle and Edwards*, 2007]. On the basis of the known source elevation of ~43 km, we assigned an offset of 41.7 km to the receiver, in order to correctly match the incidence angle of the acoustic wave at the air-ground contact. We remark that this simple numerical approach neglects acoustic refraction (minimized due to the close proximity of the instruments to the trajectory and high altitude of the source), wind, and other atmospheric effects that may produce 10–20% variability at this range.

[27] Figure 11 compares the vertical-component synthetic seismogram with the observed seismogram at site A. To facilitate comparison with the synthetic seismogram, a zero-phase band-pass filter is applied to the observed trace using a passband of 0.5–6.0 Hz. To obtain the synthetic seismogram, the Green's function output from the reflectivity algorithm was convolved with a source pulse extracted

Table 5. Near Surface Seismic Velocities and Depths at Wendover, Utah, As Determined From Shallow Hammer Seismic Refraction Survey[a]

	P Wave, m/s	*S* Wave, m/s	Layer Depth, m
Upper layer (playa)	1344 ± 73	178 ± 6	0
Lower layer (playa)	1344 ± 73	288 ± 21	5.5
Basement (carbonate rock?)	3000*	1450*	>40

[a]Asterisks indicate assumed typical value. Basement rock values shown are assumed from typical values and used for modeling purposes. Basement depth is a lower limit based on refraction data.

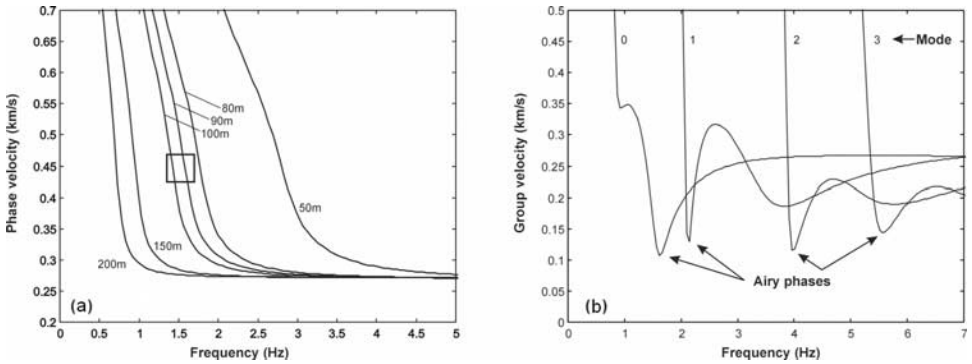

Figure 10. (a) Phase velocity dispersion curves for fundamental-mode Rayleigh waves in a three-layer model. The layer velocities and thicknesses are as in Table 5, except that the thickness of the lower soil layer (unconstrained by the seismic refraction survey) is varied as indicated and the bedrock is treated as a half space. The box shows the estimated phase velocity (0.447 ± 0.022 km/s) of the fundamental-mode Rayleigh wave in the frequency band 1.35–1.70 Hz, determined from the difference in phase spectra between sites A and B. The best fit is for an overburden thickness of 90 m. (b) Graph of group velocity for the fundamental mode Rayleigh wave (n = 0) and its first three overtones (n = 1, 2, 3). Layer parameters are the same as Figure 10a, for the 90 m thickness case. The curves reveal a set of Airy phases with similar group velocity of ∼0.12 km/s but with frequency increasing according to mode number, similar to the observed behavior (Figure 3).

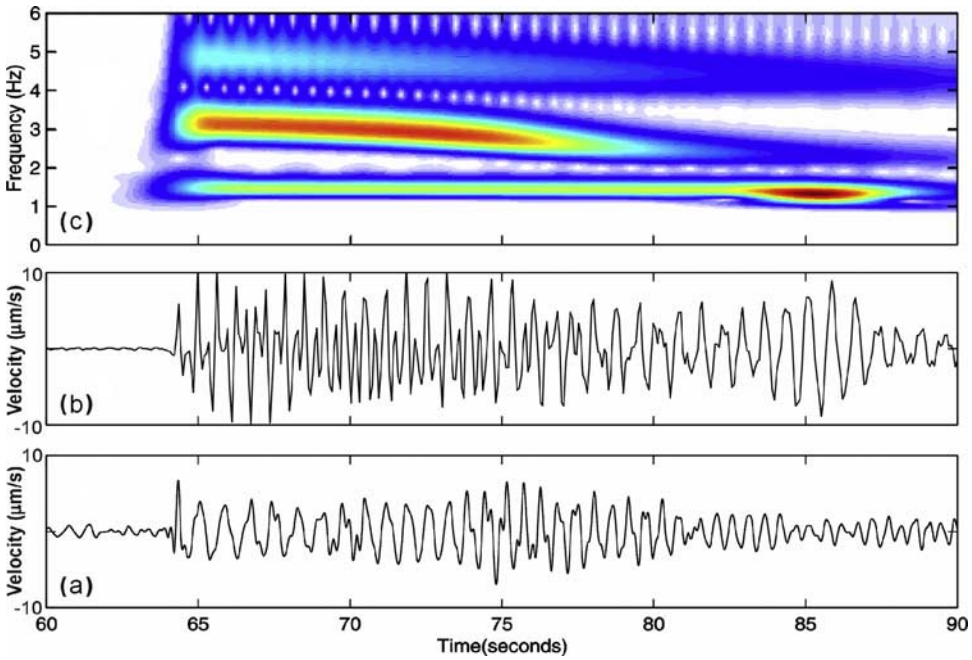

Figure 11. (a) Observed seismogram at site A, filtered using a passband of 0.5–6.0 Hz to match the synthetic results. (b) Synthetic seismogram computed using layer parameters as in Table 5, but with a lower soil layer 90 m thick and a bedrock half space. The source is treated as an explosion at an altitude of 43 km and range 41.7 km, with seismic moment $M_0 = 1.851 \times 10^7$ N-m (10% of the kinetic energy of the Stardust capsule). The Green's function was computed using a numerically stable reflectivity method [*Wang*, 1999], then converted from a point to a line source and convolved with the N wave source-time function. For this simple model, the fit with the observed trace is not exact, but the synthetic has approximately the correct pulse shape and amplitude for the initial N wave and captures many of the important characteristics of the air-coupled Rayleigh wave. (c) Time-frequency plot for the synthetic seismogram computed using the S transform. The fundamental mode (∼1.5 Hz) and first two overtones (∼3 and 5 Hz, respectively) of the Rayleigh wave are evident.

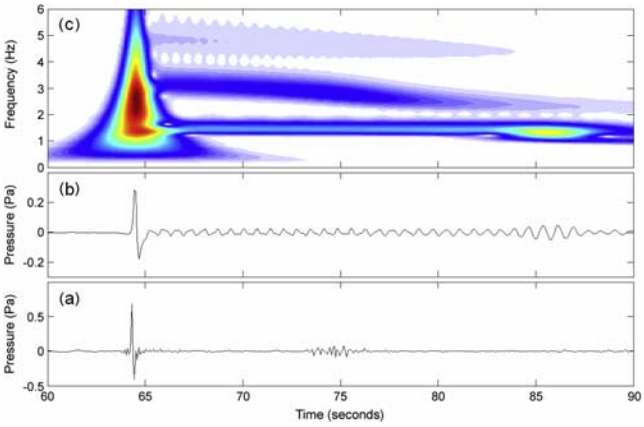

Figure 12. (a) Observed infrasonic observations at site A, filtered using a passband of 0.5–6.0 Hz to match the synthetic results. (b) Synthetic infrasonic record computed using synthetic seismogram for a seismograph located just above the station of Figure 11. Synthetic seismogram velocity was converted to pressure by multiplying by the by the "air" layer's acoustic impedance (density (0.001 kg/m^3) $\times$ sound speed (331 m/s)). (c) Time-frequency plot for synthetic infrasonic record using the *S* transform. Note the arrival of a seismic-acoustic coupled Airy phase ~20 s after the initial *N* wave, similar to the observed secondary arrival ~10 s after the Stardust *N* wave.

from the infrasound recording. In addition, the synthetic seismogram was convolved with the filter:

$$\lambda(t) = H(t)t^{-1/2} \tag{6}$$

where H is a Heaviside step function. This filter applies a correction that accounts for the pulse shape produced by a line source [*Chapman*, 2004, p. 561], rather than a point source.

[28] As shown in Figure 11, the fit between the observed and synthetic trace is not perfect, but the synthetic has approximately the correct pulse shape and amplitude for the initial *N* wave and captures many of the important characteristics of the air-coupled Rayleigh wave. For example, like the observed data, the synthetic contains a multimode air-coupled Rayleigh wave, with higher modes (overtones) that contribute higher-frequency signals and persist for ~10 s following the initial shockwave arrival.

[29] *ReVelle and Edwards* [2007] noted the difficulty in explaining the presence of the enigmatic secondary arrival from the standpoint of atmospheric propagation but nevertheless interpreted it as a likely result of multipathing. Our modeling results suggest an alternative interpretation, in which the arrivals of strong Airy phases (particularly those associated with higher-order modes) produce ground-to-air coupling that was recorded by the infrasonic microphones (Figure 12). Such a process is analogous to reports of earthquakes producing audible and infrasonic sounds [e.g., *Davison*, 1938; *Mutschlecner and Whitaker*, 2005]. Though it is apparent that some frequencies are more easily transferred back into the air, the overall frequency content in the spectra remain similar in both infrasound and seismic recordings, between 1 and 10 Hz (Figures 3a and 3b).

8. Discussion

[30] Previous studies have documented acoustic-seismic coupling in different settings. For example, sonic booms from several types of aircraft were observed by *McDonald and Goforth* [1969] at Edwards Air Force Base on both basement rock (quartz monzonite) and clay-rich playa surfaces (similar to that found at Wendover). Although the observed overpressures (10's to 100's Pa) are significantly greater than any yet recorded for a naturally occurring meteor, the dominant periods for *N* waves produced by sonic booms (0.169–0.303 s) overlap with those from natural meteors and the results of our study. The reported vertical coupling constants [*McDonald and Goforth*, 1969] for both basement rock (0.4–3.5 μm s^{-1}/Pa) and clay-rich playa (1.0–3.1 μm s^{-1}/Pa) are considerably less than those observed here.

[31] Using amplified speakers, Brüel & Kjaer microphones, and three-component geophones, a series of controlled experiments were performed by *Bass et al.* [1980] and *Sabatier et al.* [1986] to measure acoustic-seismic coupling in the 20–300 Hz frequency range. For the ground materials tested (loess, silty loam, and sandy soil), coupling strength generally varied inversely with frequency but peaked at the natural frequencies of the soil layer. At low frequencies (20–25 Hz), measured acoustic-seismic coupling values were 6–7 μm s^{-1}/Pa and 7–8 μm s^{-1}/Pa for silty loam and loess, respectively, whereas a value of 14 μm s^{-1}/Pa was found for sandy soil at 50 Hz [*Bass et al.*, 1980; *Sabatier et al.*, 1986]. These values are similar to our observations of the Stardust reentry (Table 3). In addition, good agreement was found between these experimental results and predictions made using modified Biot-Stoll poroelastic theory [*Biot*, 1956a, 1956b; *Stoll*, 1980]. This theory treats the soil layer as a two-phase medium, consisting of a solid matrix with fluid-filled pore space. Given the discrepancy between our observed seismograms and synthetics computed using linear elastic theory (Figure 11), it appears that a more complete poroelastic theory may be required to provide an accurate representation of air-soil coupling processes.

[32] Our results provide general support for previous studies that use inferred seismic observations of *N* waves to locate meteor events but also indicate that caution must be exercised in the interpretation of seismograms. Here we show that complex wave trains may be caused by air-coupled Rayleigh waves, including higher modes and prominent Airy phases. *Kanamori et al.* [1991, 1992] showed that mountainous terrain and high-rise buildings can also produce complex wave trains, which can increase the effective acoustic-seismic coupling efficiency but mask the airwave arrival. Taken together, these findings indicate that signals associated with acoustic-seismic coupling are not always a direct result of local surface loading by airwave overpressure. Thus there is not necessarily a one-to-one correspondence between seismic arrivals and airwaves from meteor events, as assumed in some previous studies.

[33] In view of the much more extensive global distribution of seismic networks than infrasound stations, it would be useful to derive a conversion formula that would enable pseudo-infrasound recordings to be computed from seismograms. By incorporating existing scaling relations for infrasound measurements, such a calibration could provide a new tool to constrain the flux of moderately sized meteoroids (0.01–1 m), which are otherwise difficult to detect. The results of this study provide some encouragement for this approach; it is clear, however, that in order to achieve a useful accuracy a high degree of certainty (within 10%, particularly for shear velocity) for near-surface properties is required. Furthermore, acoustic-seismic coupling processes are complex and further theoretical developments will be needed to improve modeling capabilities.

9. Conclusions

[34] We report colocated seismic and infrasound observations of the shockwave produced by the Stardust sample return capsule (SSRC), providing the first-ever calibrated measurement of acoustic-seismic coupling efficiency for a meteor analog. In addition to coincident arrival times and similar pulse shapes, we document good agreement between directions determined using infrasound array measurements and seismic particle-motion analysis. Near-surface characteristics of the recording site are determined using both laboratory measurements and shallow-seismic profiling. On the basis of these results, we calculate an energy admittance coefficient of 2.13% ± 0.15%, several orders of magnitude larger than values estimated in previous studies of bolide seismic observations.

[35] The pulse shape of the seismically observed *N* wave is consistent with simple calculations of acoustic overpressure loading of an elastic half-space [*Ben-Menahem and Singh*, 1981], but the amplitude is underestimated by a factor of ~2. This discrepancy may reflect amplification caused by poroelastic coupling between air and pore fluids in the soil. Following the initial *N* wave, we observe a dispersed wave train that is most likely an air-coupled Raleigh wave [*Ewing et al.*, 1957]. Ground-air coupling of higher-mode Airy phases, analogous to earthquake-generated sounds, may explain enigmatic late arrivals detected on the infrasound recordings. Further observations using colocated infrasound and seismic equipment of meteor/fireballs/bolides, or similar high-altitude hypersonic objects, will be required to explore the range of variability of acoustic-seismic coupling and its efficiency over various frequencies, surface materials, incidence angles, and geologic environments.

[36] **Acknowledgments.** The authors thank Jim Petersen and all the staff and volunteers at the Wendover airfield for their assistance during the course of this study and the two anonymous reviewers for their useful suggestions on improving the manuscript. PJM thanks Steve Hicock for the use of the grain size analysis facility at the University of Western Ontario. This work was supported by Discovery grants to DWE and PGB from the Natural Sciences and Engineering Research Council of Canada, the Canada Research Chairs Program as well as funds from the Ontario Research and Development Challenge Fund.

References

Aki, K., and P. Richards (1980), *Quantitative Seismology: Theory and Methods*, W.H. Freeman, San Francisco, Calif.

American Society for Testing and Materials (ASTM) (1972), Standard method for particle-size analysis of soils, in *Annual Book of ASTM Standards*, pp. 112–122, West Conshohocken, Pa.

Bass, H. E., L. N. Bolen, D. Cress, J. Lundien, and M. Flohr (1980), Coupling of airborne sound into the earth: Frequency dependence, *J. Acoust. Soc. Am.*, *67*, 1502–1506.

Ben-Menahem, A. (1975), Source parameters of the Siberian explosion of June 30, 1908, from analysis and synthesis of seismic signals at four stations, *Phys. Earth Planet. Int.*, *11*, 1–35.

Ben-Menahem, A., and S. J. Singh (1981), *Seismic Waves and Sources*, Springer, New York.

Biot, M. A. (1956a), Theory of propagation of elastic waves in a fluid-saturated porous solid. I. Low-frequency range, *J. Acoust. Soc. Am.*, *28*, 168–178.

Biot, M. A. (1956b), Theory of propagation of elastic waves in a fluid-saturated porous solid. II. Higher frequency range, *J. Acoust. Soc. Am.*, *28*, 179–191.

Brown, P. G., D. O. ReVelle, E. Tagiaferri, and A. R. Hildebrand (2002), An entry model for the Tagish Lake fireball using seismic, satellite and infrasound records, *Meteorit. Planet. Sci.*, *37*, 661–675.

Brown, P. G., P. Kalenda, D. O. ReVelle, and J. Borovicka (2003), The Moravka meteorite fall: 2. Interpretation of infrasonic and seismic data, *Meteorit. Planet. Sci.*, *38*, 989–1003.

Cates, J. E., and B. Sturtevant (2002), Seismic detection of sonic booms, *J. Acoust. Soc. Am.*, *111*, 614–628.

Ceplecha, Z., J. Borovicka, W. G. Elford, D. O. ReVelle, R. L. Hawkes, V. Porubcan, and M. Simek (1998), Meteor phenomena and bodies, *Space Sci. Rev.*, *84*, 327–471.

Cevolani, G., L. Foschini, and G. Trivellone (1993), The Lugo fireball of January 19, 1993, *Nuovo Cimento*, *16*, 463–471.

Chapman, C. (2004), *Fundamentals of Seismic Wave Propagation*, Cambridge Univ. Press, Cambridge, U. K.

Davison, C. (1938), Earthquake sounds, *Bulletin of the Seismological Society of America*, *28*, 147–161.

Edwards, W. N., P. G. Brown, and D. O. ReVelle (2006), Estimates of meteoroid kinetic energies from observations of infrasonic airwaves, *J. Atmos. Sol. Terr. Phys.*, *68*, 1136–1160.

Ewing, W. M., W. S. Jardetzky, and F. Press (1957), *Elastic Waves in Layered Media*, McGraw-Hill, New York.

Hildebrand, A. R., P. G. Brown, J. F. Wacker, R. J. Wetmiller, D. Pagé, D. W. E. Green, C. F. Jacobs, D. O. ReVelle, E. Tagliaferri, and S. A. Kissin (1997), The St-Robert bolide of June 14, 1994, *J. R. Astron. Soc. Can.*, *91*, 261–275.

Hunter, J. A., M. Douma, R. A. Burns, R. L. Good, S. E. Pullan, J. B. Harris, J. L. Luternauer, and M. E. Best (1998), Testing and application of near-surface geophysical techniques for earthquake hazards studies, Fraser river delta, British Columbia, in *Geology and Natural Hazards of the Fraser River Delta, British Columbia*, edited by J. J. Clague, J. L. Luternauer, and D. C. Mosher, *Geol. Surv. Can. Bull.*, *525*, 123–145.

Ishihara, Y., M. Furumoto, S. Sakai, and S. Tsukada (2004), The Kanto large bolide's trajectory determined from shockwaves recorded by a seismic network and images taken by a video camera, *Geophys. Res. Lett.*, *31*, L14702, doi:10.1029/2004GL020287.

Jenniskens, P., et al. (2006), Surface heating from the remote sensing of the hypervelocity entry of the NASA GENESIS sample return capsule, paper presented at 44th AIAA Aerospace Sciences Meeting and Exhibit, Am. Inst. of Aeron. and Astron., Reno, Nevada.

Kanamori, H., J. Mori, D. L. Anderson, and T. H. Heaton (1991), Seismic excitation by the space shuttle Columbia, *Nature*, *349*, 781–782.

Kanamori, H., J. Mori, B. Sturtevant, D. L. Anderson, and T. Heaton (1992), Seismic excitation by space shuttles, *Shock Waves*, *2*, 89–96.

Langston, C. A. (2004), Seismic ground motions from a bolide shock wave, *J. Geophys. Res.*, *109*, B12309, doi:10.1029/2004JB003167.

McCollum, L. B., and D. M. Millar (1991), Cambrian stratigraphy of the Wendover area, Utah and Nevada, *U.S. Geol. Surv. Bull.*, *1948*, 1–51.

McDonald, J. A., and T. T. Goforth (1969), Seismic effects of sonic booms: Empirical results, *J. Geophys. Res.*, *74*, 2637–2647.

Mitcheltree, R. A., R. G. Wilmoth, F. M. Cheatwood, G. J. Brauckmann, and F. A. Greene (1999), Aerodynamics of Stardust sample return capsule, *J. Spacecr. Rockets*, *36*, 429–435.

Mutschlecner, J. P., and R. W. Whitaker (2005), Infrasound from earthquakes, *J. Geophys. Res.*, *110*, D01108, doi:10.1029/2004JD005067.

Nagasawa, K. (1978), An analysis of sonic boom from a Great Fireball on May 10, 1977, recorded on seismographs of volcano observations, *Bull. Earthquake Res. Inst. Univ. Tokyo*, *53*, 271–280.

Qamar, A. (1995), Space shuttle and meteoroid—Tracking supersonic objects in the atmosphere with seismographs, *Seismol. Res. Lett.*, *66*, 6–12.

ReVelle, D. O. (1976), On meteor-generated infrasound, *J. Geophys. Res.*, *81*, 1217–1230.

ReVelle, D. O., and W. N. Edwards (2007), Stardust – An artificial, low velocity "meteor" fall and recovery: 15 January 2006, *Meteorit. Planet. Sci.*, *42*, 271–299.

ReVelle, D. O., W. N. Edwards, and T. D. Sandoval (2005), Genesis – An artificial, low velocity "meteor" fall and recovery: September 8, 2004, *Meteorit. Planet. Sci.*, *40*, 895–916.

Sabatier, J. M., H. M. Bass, L. N. Bolen, and K. Attenborough (1986), Acoustically induced seismic waves, *J. Acoust. Soc. Am.*, *80*, 646–649.

Stockwell, R. G., L. Mansinha, and R. P. Lowe (1996), Localization of the complex spectrum: The S-transform, *IEEE Trans. Signal Process.*, *44*, 998–1001.

Stoll, R. D. (1980), Theoretical aspects of sound transmission in sediments, *J. Acoust. Soc. Am.*, *68*, 1341–1350.

Tamari, S. (2004), Optimum design for the constant-volume gas pycnometer for determining the volume of solid particles, *Meas. Sci. Technol.*, *15*, 549–558.

U. S. Department of the Army (1990), Design of aggregate surfaced roads and airfields, *Tech. Manual TM 5-822-12*, Washington, D. C.

Wang, R. (1999), A simple orthonormalization method for stable and efficient computation of Green's functions, *Bull. Seismol. Soc. Am.*, *89*, 733–741.

P. G. Brown, Department of Physics and Astronomy, University of Western Ontario, 1151 Richmond Street, London, Ontario, Canada N6A 3K7.

D. W. Eaton, W. N. Edwards, and P. J. McCausland, Department of Earth Sciences, University of Western Ontario, 1151 Richmond Street, London, ON, Canada N6A 5B7. (wedwards.uwo.ca)

D. O. ReVelle, Atmospheric, Climate, and Environmental Dynamics, Meteorological Modeling Team, P. O. Box 1663, MS D401, Los Alamos National Laboratory, Los Alamos, NM 87545, USA.